
AN INTERMEDIATE VELOCITY HI CLOUD FALLING TO THE GALACTIC DISK; POSSIBLE EVIDENCE FOR LOW METALLICITY HI GAS ORIGINATED OUTSIDE THE GALACTIC DISK

**Yasuo FUKUI¹, Masako KOGA¹, Shohei MARUYAMA¹, Takahiro HAYAKAWA¹,
Ryuji OKAMOTO¹, Hiroaki YAMAMOTO¹, Kengo TACHIHARA¹, Robin
SHELTON² and Manami SASAKI³**

¹Department of Physics, Nagoya University, Chikusa-ku, Nagoya 464-8602, Japan

²Department of Physics and Astronomy, University of Georgia, Athens, GA 30602, USA

³Dr. Karl Remeis-Sternwarte, Erlangen Centre for Astroparticle Physics,
Friedrich-Alexander-Universität Erlangen-Nürnberg, Sternwartstraße 7, D-96049 Bamberg,
Germany

*E-mail: fukui@a.phys.nagoya-u.ac.jp

Received (reception date); Accepted (acceptation date)

Abstract

We found that an intermediate velocity cloud (IVC) IVC 86–36 in H I 21 cm emission shows a head-tail distribution toward the Galactic plane with marked parallel filamentary streamers, which is extended over 40 degrees in the sky. The distance of IVC 86–36 is constrained to be less than ~ 3 kpc from absorption of a background star as determined from optical spectroscopy. There is a bridge feature in velocity between the IVC and the local ISM with velocity separation of ~ 50 km s⁻¹, which may indicate dynamical interaction of the IVC with the disk. If the interaction is correct, the distance estimate d of the IVC ranges from 200 pc to 3 kpc, and the mass of the IVC head is estimated to be $7 \times 10^3 (d/1\text{kpc})^2 M_{\odot}$. The IVC shares similar properties to the Smith cloud located at 12 kpc, including the head-tail distribution, streamers, and bridge feature, while the mass of the IVC is less than ~ 0.1 of the Smith

cloud. A comparison between the H I and the *Planck/IRAS* dust emission indicates that the dust emission of IVC 86–36 is not detectable in spite of its H I column density of $2 \times 10^{20} \text{ cm}^{-2}$, indicating low metallicity of IVC 86–36 by a factor of $\lesssim 0.2$ as compared with the solar neighbor. We conclude that IVC 86–38 is an infalling cloud which likely originated in the low-metallicity environment of the Galactic halo or the Magellanic system.

Key words: Galaxy: halo — ISM: atoms — ISM: clouds — ISM: kinematics and dynamics — ISM: structure — radio lines: ISM

1 Introduction

The Galactic halo harbors a number of high- to intermediate-velocity H I clouds (HVCs and IVCs) as revealed by 21 cm H I observations (Wakker & van Woerden 1997; van Woerden et al. 2004). It has been discussed that they may be external clouds falling onto the Galaxy and are the remnant of the building blocks of the Galaxy, expelled clouds of Galactic fountains, and H I gas stripped from the Magellanic Cloud or the other objects in the Local Group (Wakker & van Woerden 1997; Blitz et al. 1999; Braun & Burton 1999; Lockman et al. 2002; Maller & Bullock 2004; Connors et al. 2006). Some of the clouds have cometary morphologies, suggesting that they are interacting with Galactic halo material (Mirabel & Morras 1990; Brüns et al. 2000; Brüns & Mebold 2004; Peek et al. 2007). It is important to better understand the physical and kinematical states of the HVCs and IVCs in order to elucidate the history and physics of the Galactic disk-halo interaction.

The Smith Cloud (Smith 1963), located toward $(l, b) = (38^\circ 67', -13^\circ 41')$ is a unique object among the HVCs (Lockman 1984; Wakker & van Woerden 1997). It was shown that the Smith cloud is interacting with the disk H I gas based on 21 cm H I observations (Lockman et al. 2007). The cloud shows unique signatures of interaction with the Galactic halo material, including filamentary parallel features with a head-tail structure as revealed by the Green Bank Telescope (GBT). Multiple origins of the cloud have been proposed in the literature (Bland-Hawthorn et al. 1998; Sofue et al. 2004). A recent scenario under intensive attention is a cloud falling through the Galactic halo after a passage through the disk ~ 70 Myr ago, where dark matter may play a role in confining the cloud (Nichols & Bland-Hawthorn 2009), whereas the hypothesis is not supported by the hydrodynamical numerical simulations (Galyardt & Shelton 2016). The Smith cloud is located below the galactic plane ($z \sim 3$ kpc) at a distance of 12.4 ± 1.3

kpc from the sun and the total HI mass is estimated to be more than $10^6 M_{\odot}$. The metallicity of the Smith cloud is measured to be sub-solar but is still not inconsistent with the metallicity of the Galactic disk (Fox et al. 2016). Its origin may be explained by the Galactic fountain model where the disk HI gas is ejected out of the plane by supershells, the collective effects of supernovae.

IVCs are already well studied in HI at low resolution. The Pegasus-Pisces Arch (Wakker 2001) harbors several IVCs with elongated distributions. In the course of a study of the region (Fukui et al. 2014), we made a detailed analysis of the HI data taken as part of the GALFA survey (Peek et al. 2011) with the Arecibo telescope at $4'$ resolution. In this paper we present the results of the HI analysis toward an IVC in the Pegasus-Pisces Arch.

2 Results of the HI distribution

2.1 Observational data

We use the archival datasets of the Galactic Arecibo L-Band Feed Array (GALFA)-HI survey. The GALFA-HI survey data (Peek et al. 2011) is taken with the Arecibo 305 m radio telescope. Its angular resolution is $4'$ and rms noise level is 60–140 mK at 0.2 km s^{-1} velocity resolution in T_{MB} scale which is the Main Beam antenna temperature.

2.2 Spatial distribution of the IVC

We present the intermediate velocity HI cloud at $(l, b) = (86^{\circ}, -36^{\circ})$, IVC 86–36, in the Pegasus-Pisces Arch, where the name in Galactic coordinates is tentatively adopted for convenience in the present paper. The velocity with respect to the local standard of rest (LSR) is given in the present paper. Figure 1 shows a typical HI profile toward the IVC in velocity and shows that there are two velocity components; one is the local emission in a low velocity range from -20 km s^{-1} to $+10 \text{ km s}^{-1}$ and the other is peaked at large negative velocity around -45 km s^{-1} . This negative velocity component is IVC 86–36, which is apparently linked with the local HI gas by a smooth bridge-like feature as described later.

Figure 2 shows a large scale distribution of IVC 86–36, which is extended as a thin and straight feature in a region of $(l, b) = (85^{\circ}\text{--}120^{\circ}, -60^{\circ}\text{--}-30^{\circ})$. The velocity of the IVC ranges from less than -60 km s^{-1} to -20 km s^{-1} . Figure 3 shows an image of the bright HI 21 cm emission from -80 km s^{-1} to $+30 \text{ km s}^{-1}$ as velocity channel distributions. IVC 86–36 is seen from -80 km s^{-1} to -30 km s^{-1} as the straight feature from $(l, b) = (84^{\circ}, -34^{\circ})$ to $(110^{\circ}, -55^{\circ})$. The angle of the elongated IVC relative to the Galactic plane is ~ 45 degrees. IVC

86–36 has a head-tail distribution whose head, the compact brightest part, lies toward $(l, b) = (84^\circ\text{--}90^\circ, -40^\circ\text{--}-34^\circ)$. The bridge is seen in $-30 \text{ km s}^{-1} - -20 \text{ km s}^{-1}$. At velocity from -20 km s^{-1} to 10 km s^{-1} the local HI gas is dominant and we do not see the IVC. Figure 4 presents the first moment distribution calculated in a velocity range from -70 km s^{-1} to -30 km s^{-1} , showing that the red-shifted tail at velocity larger than -60 km s^{-1} has “winding” distribution as depicted by a dashed line in Figure 4, whereas the blue-shifted tail at velocity smaller than -60 km s^{-1} holds the straight distribution.

The present region includes high latitude molecular clouds MBM53–55 (Magnani et al. 1985). HI distribution was already studied at lower resolution of $30'$ by Yamamoto et al. (2003) for a velocity range of -20 km s^{-1} to $+10 \text{ km s}^{-1}$, and the major velocity component of HI associated with the CO cloud was revealed, which correspond to the HI from -11 km s^{-1} to $+1 \text{ km s}^{-1}$.

2.3 A possible kinematic signature of interaction between the IVC and the local gas

In order to obtain an insight into the relationship between the IVC and the disk, in Figure 5 we present position-velocity diagrams toward the IVC head. In Figure 5(a) we present a Galactic longitude-velocity diagram toward the IVC head, where the bridge feature is found at $-30 \text{ km s}^{-1} - -20 \text{ km s}^{-1}$ for a Galactic longitude range from 85° to 90° over the extent of the intense part of the IVC head at $\sim -40 \text{ km s}^{-1}$. In Figure 5(b) a Galactic latitude-velocity diagram in the IVC head is shown. We find the bridge feature in a Galactic longitude range from -40° to -37° . Numerical simulations of two colliding clouds indicate formation of such bridges between the two clouds (Takahira et al. 2014; Fukui et al. 2018b), and the distribution of the bridge is consistent with that IVC 86–36 is interacting with the disk HI. It is possible that the HI disk have a vertical extent of more than 3 kpc as shown by the bridge features toward the Smith cloud (Lockman et al. 2007). The similar extents of the bridge and the IVC head suggest physical connection of the IVC and the local gas.

3 Distance and mass of the IVC

3.1 Distance

It is difficult to derive the distance of IVCs which do not follow the Galactic rotation and probably have a significant radial motion to the Galactic disk. In the following we present and discuss a few possible ways of distance estimate and their uncertainties.

Stellar absorption: IVCs are generally believed to be closer to the Galactic plane than

HVCs and are located at a z -distance around 1 kpc (e.g., Clarke et al. 2001; Richter 2017). A secure limit for the distance of IVC 86–36 is obtained by absorption toward background stars. HD 215733 is located toward the head of IVC 86–36 at Galactic coordinates of $(l, b)=(85^\circ 2, 36^\circ 4)$. The distance of HD 215733 is estimated to be 2900 pc based on a spectral type of B1 II, $V = 7.3$, $E(B - V) = 0.10$, and $M_V = -5.3$ (Walborn 1976; Mermilliod 1987; Fitzgerald 1970; Lesh 1968). Recent measurements by GAIA obtained 3.5 ± 0.9 kpc as a distance of HD215733, which is consistent with the previous determination above. Another constraint on the distance was obtained to be less than 1050 pc (see Wakker 2001) by the optical absorption measurement toward a star PG0039+049 at $(l, b) = (119^\circ, 58^\circ)$ in part of the tail of IVC 86–36 (Wakker 2001; Centurion et al. 1994).

A_V estimation by stars observed with GAIA: HI column density N_{HI} is estimated to be $2 \times 10^{20} \text{ cm}^{-2}$ for the HI peaks of IVC 86–36 by assuming that the HI is optically thin. This N_{HI} corresponds to $A_V = 0.1$ mag (Draine 2011) if the Galactic gas to dust ratio is assumed to be the same in IVC 86–36. GAIA DR2 presented the most extensive catalog of stars with their parallax and other stellar properties (Gaia Collaboration 2018). We made an analysis of A_V toward IVC 86–36 as described in the Appendix and found that A_V is enhanced by ~ 2 mag at a distance of 100–200 pc, which corresponds to the local molecular clouds MBM53–55 with an HI envelope. This is consistent with the results by PS1 photometry (Schlafly et al. 2014). For the rest of the line of sight we found no enhanced A_V with a upper limit of $A_V \sim 0.3$ mag within ~ 1 kpc. The GAIA DR2 data are not sensitive enough to detect such small A_V of the IVC and the distance estimate for IVC 86–36 is not constrained with GAIA DR2.

X-ray shadow: Another possibility is to use the soft X-rays at around 1/4 keV observed with ROSAT to identify shadow due to X-ray absorption. Such X-ray absorption by the ISM is mainly due to hydrogen and helium with a possible contribution of heavy atoms at high energy above 0.5 keV. This method was successful in identifying the X-ray shadow of the Draco cloud (Burrows & Mendenhall 1991; Snowden et al. 1991). We find possible shadow candidates toward MBM53–55 in the catalog of Snowden et al. (2000) as given in Appendix 2. Some of the cataloged shadows may correspond to IVC 86–36, whereas W_{HI} of the IVC is a factor of 3–5 smaller than that of the local HI gas. It is possible that the soft X-ray background is mainly due to the Local Bubble distributed within 200 – 300 pc, making the shadow not very distinct. The 3D distribution of the soft X-ray emitting hot gas of the Local Bubble is not accurately established. A quantitative analysis of the shadows may include large uncertainties at best and we did not attempt to derive a distance of IVC 86–36 by using the X-ray shadows.

Morphology of IVC 86–36: The IVC morphology may provide another hint on the

location of the cloud. The negative velocity of IVC 86–36 indicates that the IVC is approaching the sun. If the tail was created by the interaction between the head and the halo material, it is likely that the tail is placed at a larger distance than the head. The head then conflicts with 1 kpc of PG0039+049, if the intermediate velocity gas toward PG0039+049 is a physical extension of IVC 86–36. The distance 3 kpc may not be favored in the configuration.

In summary, the distance of IVC 86–36 is still uncertain observationally and we shall consider three distances, 200 pc, 1 kpc, and 3 kpc, in the following discussion.

3.2 Cloud size and mass

We assume in the following that the tail of the cloud is at the same projected distance with the head in the disk for simplicity. Under the assumption, the head is at a distance of d and the edge of the tail is at $d \cos(36^\circ) / \cos(60^\circ) = 1.62d$. By considering the extremely straight distribution of IVC 86–36 in the sky, we assume that the cloud is straight in the 3-dimensional space. This is a natural configuration if the tail was produced by the interaction between the IVC head and the halo material at a relative velocity of $\sim 100 \text{ km s}^{-1}$. The real length of the cloud L , separation between IVC head and tail, is calculated as $L = 0.66d$, where d stands for the distance of the head. The length of the tail is calculated as $L = 130 \text{ pc}$, 660 pc and 2 kpc , for a distance of 200 pc, 1 kpc and 3 kpc, respectively.

The low brightness of the HI emission suggests that the emission is optically thin (Fukui et al. 2014), and we estimate the HI mass under the optically thin approximation by equation (2).

$$M_{\text{HI}} = \mu m_{\text{H}} \sum \left[d^2 \Omega X_{\text{HI}} W_{\text{HI}} \right] \quad (1)$$

where d is the distance of the IVC, ω is the solid angle per pixel, $X_{\text{HI}} = 1.823 \times 10^{18} [\text{cm}^{-2} \text{K}^{-1} \text{km}^{-1}]$ s is a theoretical conversion factor between the integrated intensity (W_{HI}) and the column density of HI. The total HI mass is estimated to be $7300 \times (d/1 \text{ kpc})^2 M_{\odot}$ including He mass, 1/3 of H (taken into account in = 1:33). The mass of IVC 86–36 is estimated to be $260 M_{\odot}$ to $7 \times 10^4 M_{\odot}$, which is significantly smaller than that of the Smith cloud whose mass is more than $10^6 M_{\odot}$ (Lockman et al. 2007).

4 Gas to dust ratio in IVC 86–36

In order to pursue the origin of an IVC, it is important to measure the metallicity. IVCs may have lower metallicity if they originate outside the disk, e.g., in the Magellanic system or in the Galactic halo. Metal abundance in the gas phase of IVC 86–36 was measured by optical atomic

absorption lines toward HD215733 by Fitzpatrick & Spitzer (1997) and depletion of some heavy elements are measured in a velocity range of the IVC. These measurements, however, may not directly indicate the metallicity of IVC 86–36 because of the uncertainty in assessing the atomic ionization states and the interstellar depletion due to adsorption onto dust surfaces.

Another method to measure metallicity is the dust emission or extinction which reflects dust abundance. The most sensitive observations of the dust emission at sub-mm wavelengths are obtained by the combined *Planck*/*IRAS* data. Figure 6 shows the distributions of radiation toward the region of IVC 86–36. Figure 6(a)-1 shows the distribution of the dust optical depth at 353 GHz τ_{353} and Figure 6(a)-2 the distribution of the dust temperature T_d . These two quantities are derived by fitting a modified Planck function at three wavelengths of the *Planck* data, 850, 550 and 350 μm (corresponding to frequencies of 353, 545 and 857 GHz) (Planck Collaboration 2014a), in addition to the *IRAS* 100 μm data (Schlegel et al. 1998; Miville-Deschênes & Lagache 2005). The *IRAS* data were smoothed to the beam size of the *Planck* data 5'. The dust emissivity is expressed as $I_\nu = \tau_{353} B_\nu(T_d)(\nu/353 \text{ GHz})^\beta$ where a coefficient β were simultaneously fit with τ_{353} and T_d . For more details see Planck Collaboration (2014b).

Figure 6(b)-1 shows in gray scale the distribution of the integrated intensity of the local HI emission in a velocity range of -30 – $+30 \text{ km s}^{-1}$, and Figure 6(b)-2 the distribution of the IVC HI emission in a velocity range of -60 – -30 km s^{-1} . The white thick contours in Figures 6(a)-1, (a)-2 and (b)-1 show the outer contour of the IVC at an intensity level of 30 K km s^{-1} . The white contours in Figure 6(b)-2 are the HI intensity of the local ISM in Figure 6(b)-1 at an intensity level of 260 K km s^{-1} . The thin contours in Figure 6(a)-2 shows the CO distribution at 3.4 K km s^{-1} of the local ISM in a velocity range of -12 – $+2 \text{ km s}^{-1}$. τ_{353} is a sum of the contributions of both the local ISM and the IVC. The main HI cloud (Figure 6(b)-1) that includes the high latitude molecular clouds MBM53–55 observed in CO (Figures 6(a)-2) is distributed in a velocity range of the local ISM from the northeast to the southwest and the distribution is similar to τ_{353} (Figure 6(a)-1). The HI distribution is extended outside the molecular cloud and shows weaker τ_{353} than the main cloud (Figures 6(a)-1 and 6(b)-1). We note that IVC 86–36 (Figure 6(b)-2) shows no appreciable enhancement of τ_{353} (Figure 10(a)-1) or no correlated variation in T_d (Figure 6(a)-2) for W_{HI} of the IVC $\sim 200 \text{ K km s}^{-1}$. N_{HI} of the IVC head corresponds to sub-mm dust optical depth $\tau_{353} = 3 \times 10^{-6}$ according to the works on the *Planck*/*IRAS* dust properties (Planck Collaboration 2014b; Fukui et al. 2014; Fukui et al. 2015). This suggests that IVC 86–36 has a significantly smaller dust optical depth than the local ISM.

Figure 7 shows a scatter plot between τ_{353} and W_{HI} of the local ISM for τ_{353} above

2×10^{-6} , where the dust temperature derived from the *Planck/IRAS* data T_d is shown by the color code. T_d is positively correlated with the HI spin temperature T_s because the both temperatures reflect heating by UV of the ISRF, and T_s increases with the increase of T_d ; HI heating by the photoelectric effect and dust heating by the UV absorption. The both temperatures differ substantially from each other because collisional coupling between HI and dust is too weak to equalize their temperatures in the usual CNM (Draine 2011). Due to the strong T_d dependence of the dust radiation energy as expressed by T_d^6 , T_d ranges from 16 to 22 K (Planck Collaboration 2014b) and T_s from 10 K to 10^4 K (e.g., Fukui et al. 2018a). τ_{353} is a sum of the foreground ISM and the IVC. In order to quantify the gas/dust ratio of IVC 86–36 we subtract the contribution of the foreground ISM and derive τ_{353} of the IVC. In the present region Fukui et al. (2014) showed that the HI gas with T_d higher than 21 K is optically thin and W_{HI} is proportional to N_{HI} with a small dispersion of less than 10 % in that T_d range. The reason for the small dispersion is the small HI optical depth less than ~ 0.2 at the highest temperature, where the optically thin approximation is valid for the HI emission. A similar trend is also found for the local ISM in most of the high b region within 200 pc of the sun (Fukui et al. 2014; Fukui et al. 2015). This suggests that the local HI gas with the highest T_d shows the best correlation and is thus suited for accurate foreground subtraction in W_{HI} .

Figure 8 shows a set up for the foreground subtraction toward IVC 86–36. We chose two areas for the present analysis. One is the area of the IVC head and the other the reference area surrounding the head with very weak HI emission of IVC 86–36. We masked regions with T_d lower than 20 K where HI optical depth becomes larger than 0.2, and those with strong point sources where τ_{353} is contaminated by the infrared radiation of the point sources. We note that the dust temperature measured by the *Planck/IRAS* shows significant increase toward IVC 86–36 due to the extragalactic source 3C 454.3 (Abdo et al. 2009). If the foreground HI emission is uniform over the area in Figure 8, we are able to accurately subtract the foreground τ_{353} calculated from W_{HI} of the local ISM. Figure 9 shows scatter plots between τ_{353} and W_{HI} for $T_d = 20.0 - 20.5$ K and for T_d higher than 20.5 K in the reference area and the area of the head. In all the panels of Figure 9 we see positive correlation with dispersion of ~ 25 % or less in τ_{353} . The foreground ISM is therefore dominant in τ_{353} and is fairly uniformly distributed over the region shown in Figure 8. We expect that τ_{353} of IVC 86–36 is obtained by subtracting the reference τ_{353} from the total τ_{353} .

The result of the subtraction is shown as a τ_{353} - W_{HI} plot for the subtracted τ_{353} and W_{HI} of the IVC in Figure 10. This indicates that the IVC shows significantly smaller τ_{353} than the local ISM. Linear regressions are obtained as follows for $T_d > 20.5$ K;

$$\text{the IVC: } W_{\text{HI}}(\text{K km s}^{-1}) = (2.6 \pm 0.2) \times 10^8 \tau_{353} + (105 \pm 4), \quad (2)$$

and

$$\text{the local ISM: } W_{\text{HI}}(\text{K km s}^{-1}) = (5.6 \pm 0.2) \times 10^7 \tau_{353} + (31 \pm 7), \quad (3)$$

where the errors are the standard deviation obtained through the linear regression. By taking a ratio of the two slopes we obtain 0.22 ± 0.02 as an upper limit for the difference of the IVC relative to the local ISM. If the dust optical depth is assumed to be proportional to the metallicity, this indicates that IVC 86–36 has a significantly smaller metallicity than the solar value in the local gas.

5 Discussion: Falling-cloud scenario

We present a possible scenario of IVC 86–36. The head-tail distribution suggests that the IVC is moving toward the Galactic plane. It is a natural interpretation that the tail and streams were formed via dynamical interaction between the head and the halo material as shown by hydrodynamical numerical simulations for the Smith cloud (Galyardt & Shelton 2016), and the tail is located behind the head which is moving toward us. The falling velocity of the IVC is at least $\sim 60 \text{ km s}^{-1}$ by assuming the cloud motion with an angle of 45 degrees to the line of sight. The distance of IVC 86–36 is weakly constrained to be from 3 kpc to 200 pc by the stellar absorption lines and the tentative dynamical interaction signatures if real (Section 3). If we assume a z -distance of 1 kpc typical to IVCs, the dynamical timescale of IVC 86–36 is estimated to be $\sim 1 \text{ kpc}/60 \text{ km s}^{-1} \sim 20 \text{ Myrs}$.

The Smith cloud shares these properties with IVC 86–36, which are interpreted as dynamical interaction signatures (Lockman 2003). The distance of the Smith cloud is 12 kpc, more distant than IVC 86–36, and its total mass is in excess of $10^6 M_{\odot}$ significantly larger than IVC 86–36. The dynamical impact of IVC 86–36, e.g., the angular momentum increase as well as mass input to the Galaxy, is therefore less dramatic than the Smith cloud. The heavy element abundance of the Smith cloud is not so anomalous as compared with the Galactic disk; absorption measurements of a sulfur spectrum argues for a Galactic disk origin of the Smith cloud, such as gas on the returning point of a fountain (Bregman 1980) launched into the halo at some location in the disk (Sofue et al. 2004). Absorption line measurements toward the bright star HD215733 in IVC 86–36 at $(l, b) = (85^{\circ}, -36^{\circ})$ (Figure 2) were made at ultraviolet wavelengths by Fitzpatrick & Spitzer (1997). These authors found a trend that heavy atoms toward IVC 86–36 show subsolar abundance while it may be affected by the atomic ionization

states and interstellar depletion. It was thus not clear if IVC 86–36 originated outside the high-metallicity Galactic disk in the previous works.

The present analysis revealed that the dust optical depth of IVC 86–36 is less than $\sim 20\%$ as compared with that in the solar vicinity, indicating that the metal abundances of IVC 86–36 are less than ~ 0.2 solar. Dust optical depth at sub-mm wavelength provides a measure of heavy elements that are not affected by the interstellar atomic depletion or the ionization states as long as the dust destruction process is not effective. The interstellar shocks may affect dust destruction while the time scale is as large as 100 Myrs for large grains (e.g., Barlow & Silk 1977; Dwek & Scalo 1979; Dwek & Scalo 1980; Draine & Salpeter 1979b; Draine & Salpeter 1979a). It is therefore unlikely that dust destruction is important in IVC 86–36.

The origin of IVC 86–36 is of considerable interest and the metal abundances are one of the clues to pursue it. The Magellanic Stream as well as many HVCs have metallicity in the order of ~ 0.1 solar according to optical observations toward bright background sources (see for a review D’Onghia & Fox 2016 and references therein). The present work showed that the metal abundances of IVC 86–36 are less than 0.2 solar and suggest that IVC 86–36 is not explained by the Galactic fountain model. IVC 86–36 is located in the southern sky, and the Magellanic system may be a reasonable origin of IVC 86–36. The Magellanic Stream or the SMC shows similar low metal abundance of 0.1–0.2 solar (D’Onghia & Fox 2016). The previous measurements of metal abundances were limited almost solely to the optical absorption toward compact sources in the preceding works, while the method samples a very small volume of the gas. A large number of the background sources will help improve this deficiency. The far infrared/sub-mm dust emission may expand the sampled volume as shown in the present work. Fong et al. (1987) used *IRAS* 100 micron emission toward the Magellanic Stream in order to quantify dust abundance in the Magellanic Stream, whereas the low sensitivity did not allow the authors to derive reliable dust abundance (see their Figure 4). Recently, the *Planck/IRAS* data at sub-mm to 100 micron were used to derive dust abundance in the LMC and a significant variation of dust abundance was revealed in the HI ridge of the LMC, lending support for mixing of gas with different metal abundances between the LMC and SMC, which was driven by tidal interaction between the two galaxies (Fukui et al. 2017). The present work applied the same method with these authors and showed that the *Planck/IRAS* data have a potential to study dust abundance in HVCs and IVCs.

The possible physical process of the interaction of IVC 86–36 is a subject of considerable interest. The formation of the long tail is probably due to the past interaction between the IVC and the halo, and the interaction is not directly detected at present. As an example of

the interaction, we find a ripple in the tail in a range from -55 km s^{-1} to -40 km s^{-1} at $l = 110^\circ\text{--}90^\circ$ (Figure 4), which may suggest some instability in the frictional interaction. The falling velocity may create shock fronts also, while we do not see signs of X-rays or thermal emission from shocked gas possibly due to cooling (Condon et al. 1998). There is no detectable CO toward IVC 86–36 (Figure 6). This requires physical modeling of the interaction while it is beyond the scope of the present paper. It is highly desirable to make hydrodynamical numerical simulations of IVC 86–36 in the Galactic disk. Questions to be answered by hydrodynamical simulations include (1) the dynamical interaction with the halo medium including heating, (2) constraints on the cloud orbit, and (3) cloud confinement and the possible role of the magnetic field, and (4) assessment of possible merging of the falling clouds into the Galactic disk.

6 CONCLUSIONS

We have analyzed the Arecibo HI data and found that an intermediate velocity cloud IVC 86–36 is falling onto the Galactic plane within 3 kpc of the sun. The main conclusions are summarized below.

IVC 86–36 shows an intensity distribution consisting of a head-tail structure, and the tail is elongated over 40 degrees in the sky at an apparent angle of $\sim 45^\circ$ to the Galactic plane. It is likely that IVC 86–36 is falling to the Galactic plane in a timescale of ~ 20 Myrs as estimated from a ratio of the length of the tail and the velocity, $1 \text{ kpc}/60 \text{ km s}^{-1}$, for an assumed distance of 1 kpc. Several parallel filamentary features streaming along the head-tail direction comprise the tail and are probably formed by the dynamical interaction between the IVC and the halo material. Possible signatures of such interaction are shown by the bridge features etc. which are connecting IVC 86–36 and the disk. The distance of IVC 86–36 is not well constrained, while stellar absorption places IVC 86–36 at a distance closer than 1–3 kpc. The distance estimates are not in conflict with the GAIA DR2 data or soft X-ray shadows due to absorption. The HI mass of IVC 86–36 is estimated to be $7300 \times (d/1\text{kpc})^2 M_\odot$ under the optically thin approximation of the HI emission. We analyzed the HI and *Planck/IRAS* data and found that the dust optical depth τ_{353} is too small to be detectable toward IVC 86–36. For the local ISM we derived a linear relationship between W_{HI} and τ_{353} with an accuracy better than 10 %, and we used the relationship in order to make a subtraction in τ_{353} of the foreground component, the local ISM, toward IVC 86–36 and derived an upper limit of the dust to HI ratio to be less than ~ 0.2 solar. This indicates that IVC 86–36 originated in a low metallicity environment like the Magellanic system or the halo, but not in the disk via the fountain model

where the high metallicity ISM circulates in the disk. The morphological and kinematical properties of IVC 86–36 are similar to the Smith cloud which is located 12 kpc away from the solar system. An important difference from the Smith cloud is the low metallicity of IVC 86–36 which suggests origin of the IVC belongs to the low metallicity environment. Detailed hydrodynamical numerical simulations of the interaction are crucial to shed more light on the physical processes of such falling gas.

Acknowledgments

This work was supported by Grants-in-Aid for Scientific Research (KAKENHI) of the Japan society for the Promotion of Science (JSPS) Grant Numbers 15H05694, 25287035. This publication utilizes data from Galactic ALFA HI (GALFA HI) survey data set obtained with the Arecibo L-band Feed Array (ALFA) on the Arecibo 305 m telescope. Arecibo Observatory is part of the National Astronomy and Ionosphere Center, which is operated by Cornell University under Cooperative Agreement with the U.S. National Science Foundation. The GALFA surveys are funded by the NSF through grants to Columbia University, the University of Wisconsin, and the University of California. Some of the results in this paper have been derived using the HEALPix (Górski et al. 2005) package. The useful comments by the referee helped to improve the content and readability of the paper.

Appendix 1 Distance estimate by GAIA DR2

GAIA is an all-sky survey mission for astrometry, and the data are useful to constrain the distance of interstellar clouds. In addition to the parallax measurements, GAIA DR2 (Gaia Collaboration 2018) provides broadband photometric data of about one billion stars, giving G magnitude integrated over the passband of $\sim 330 - 1050$ nm, as well as the low-resolution prism spectra of BP and RP (Evans et al. 2018). For stars brighter than $G = 17$ mag, stellar effective temperatures, T_{eff} , are obtained from the photometric data by adopting stellar color models (Andrae et al. 2018). It also gives line-of-sight extinctions A_G by using the parallaxial distances, and the reddening $E(\text{BP} - \text{RP})$. We try to estimate the distance to the IVC cloud from the A_G and distances of stars in the directions of high HI intensity. We chose 3 test fields with $10'$ radius centered at $(l, b) = (84^\circ.7024, -34^\circ.1755)$, $(85^\circ.9251, -37^\circ.0801)$, and $(84^\circ.5516, -37^\circ.3366)$ toward peak positions of HI intensity where the HI is dominated by the IVC component with radial velocity of $-60 - -30$ km s $^{-1}$. For comparison, we also chose 4 fields at $(l, b) = (89^\circ.9009, -33^\circ.4960)$, $(93^\circ.9883, -33^\circ.1297)$, $(94^\circ.6707, -35^\circ.0790)$, and $(95^\circ.4079, -35^\circ.6351)$ in MBM 53 where the HI is dominated by the local cloud at ~ 0 km s $^{-1}$. The total numbers of GAIA sources selected from the 3 fields toward the IVC and the 4 fields toward MBM 53 are 1571 and 2024, respectively. Figure 11 plots the extinction A_G against the distance for the GAIA sources sampled from the fields in the IVC (filled circles) and in MBM 53 (open circles). A_G is

expected to increase with distance if the interstellar dust distributes uniformly, while it jumps if a dense interstellar cloud is located at a particular distance. For the stars in MBM 53, a noticeable jump of A_G by ~ 1 mag is seen around $d \sim 250$ pc, which nicely corresponds to the distance of MBM 53 derived by Schlafly et al. (2014). For those in the IVC, on the other hand, A_G slowly increases with distance, but no clear jump is observed. These imply that the IVC is either located farther away than 500 pc, or consist of ISM with less dust grains (i.e, metal poor condition) resulting in lower extinction.

Appendix 2 X-ray shadows from the ROSAT data

The HI distributions of the local HI gas and IVC 86–36 were compared with the soft X-ray (1/4 keV) distribution observed with ROSAT (Snowden et al. 1997). Figure 12(a) shows an overlay with the local gas and Figure 12(b) with the IVC. The circles are taken from a list of soft X-ray shadows identified by Snowden et al. (2000) and the names are taken from the list. The local gas shows rough correspondence with some of the shadows, whereas the IVC shows marginal correspondence with the shadows. It is possible that the local gas is responsible for the shadowing, although the contribution of the IVC to the shadows is uncertain.

References

- Abdo, A. A., et al., 2009, ApJ, 699, 817
- Andrae, R., et al., 2018, A&A, 616, A8
- Barlow, M. J., & Silk, J., 1977, ApJL, 211, L83
- Bland-Hawthorn, J., Veilleux, S., Cecil, G. N., Putman, M. E., Gibson, B. K., & Maloney, P. R., 1998, MNRAS, 299, 611
- Blitz, L., Spergel, D. N., Teuben, P. J., Hartmann, D., & Burton, W. B., 1999, ApJ, 514, 818
- Braun, R., & Burton, W. B., 1999, A&A, 341, 437
- Bregman, J. N., 1980, ApJ, 236, 577
- Brüns, C., Kerp, J., Kalberla, P. M. W., & Mebold, U., 2000, A&A, 357, 120
- Brüns, C., & Mebold, U., 2004, in H. van Woerden, B. P. Wakker, U. J. Schwarz, & K. S. de Boer, eds., High Velocity Clouds, *Astrophysics and Space Science Library*, volume 312, 251
- Burrows, D. N., & Mendenhall, J. A., 1991, Nature, 351, 629
- Centurion, M., Vladilo, G., de Boer, K. S., Herbstmeier, U., & Schwarz, U. J., 1994, A&A, 292, 261

- Clarke, T. E., Gladders, M., & Mallén-Ornelas, G., 2001, in J. E. Hibbard, M. Rupen, & J. H. van Gorkom, eds., Gas and Galaxy Evolution, *Astronomical Society of the Pacific Conference Series*, volume 240, 529
- Condon, J. J., Cotton, W. D., Greisen, E. W., Yin, Q. F., Perley, R. A., Taylor, G. B., & Broderick, J. J., 1998, *AJ*, 115, 1693
- Connors, T. W., Kawata, D., Bailin, J., Tumlinson, J., & Gibson, B. K., 2006, *ApJL*, 646, L53
- D’Onghia, E., & Fox, A. J., 2016, *ARA&A*, 54, 363
- Draine, B. T., 2011, *Physics of the Interstellar and Intergalactic Medium* (Princeton, NJ: Princeton University Press)
- Draine, B. T., & Salpeter, E. E., 1979a, *ApJ*, 231, 438
- Draine, B. T., & Salpeter, E. E., 1979b, *ApJ*, 231, 77
- Dwek, E., & Scalo, J. M., 1979, *ApJL*, 233, L81
- Dwek, E., & Scalo, J. M., 1980, *ApJ*, 239, 193
- Evans, D. W., et al., 2018, *A&A*, 616, A4
- Fitzgerald, M. P., 1970, *A&A*, 4, 234
- Fitzpatrick, E. L., & Spitzer, Jr., L., 1997, *ApJ*, 475, 623
- Fong, R., Jones, L. R., Shanks, T., Stevenson, P. R. F., & Strong, A. W., 1987, *MNRAS*, 224, 1059
- Fox, A. J., et al., 2016, *ApJL*, 816, L11
- Fukui, Y., Hayakawa, T., Inoue, T., Torii, K., Okamoto, R., Tachihara, K., Onishi, T., & Hayashi, K., 2018a, *ApJ*, 860, 33
- Fukui, Y., Torii, K., Onishi, T., Yamamoto, H., Okamoto, R., Hayakawa, T., Tachihara, K., & Sano, H., 2015, *ApJ*, 798, 6
- Fukui, Y., Tsuge, K., Sano, H., Bekki, K., Yozin, C., Tachihara, K., & Inoue, T., 2017, *PASJ*, 69, L5
- Fukui, Y., et al., 2014, *ApJ*, 796, 59
- Fukui, Y., et al., 2018b, *ApJ*, 859, 166
- Gaia Collaboration, 2018, *A&A*, 616, A1
- Galyardt, J., & Shelton, R. L., 2016, *ApJL*, 816, L18
- Górski, K. M., Hivon, E., Banday, A. J., Wandelt, B. D., Hansen, F. K., Reinecke, M., & Bartelmann, M., 2005, *ApJ*, 622, 759
- Lesh, J. R., 1968, *ApJS*, 17, 371
- Lockman, F. J., 1984, *ApJ*, 283, 90
- Lockman, F. J., 2003, *ApJL*, 591, L33
- Lockman, F. J., Benjamin, R. A., Heroux, A., & Langston, G. I., 2007, in American Astronomical Society Meeting Abstracts, *Bulletin of the American Astronomical Society*, volume 39, 1000

Lockman, F. J., Murphy, E. M., Petty-Powell, S., & Urick, V. J., 2002, *ApJS*, 140, 331

Magnani, L., Blitz, L., & Mundy, L., 1985, *ApJ*, 295, 402

Maller, A. H., & Bullock, J. S., 2004, *MNRAS*, 355, 694

Mermilliod, J.-C., 1987, *A&AS*, 71, 119

Mirabel, I. F., & Morras, R., 1990, *ApJ*, 356, 130

Miville-Deschênes, M.-A., & Lagache, G., 2005, *ApJS*, 157, 302

Nichols, M., & Bland-Hawthorn, J., 2009, *ApJ*, 707, 1642

Peek, J. E. G., Putman, M. E., McKee, C. F., Heiles, C., & Stanimirović, S., 2007, *ApJ*, 656, 907

Peek, J. E. G., et al., 2011, *ApJS*, 194, 20

Planck Collaboration, 2014a, *A&A*, 571, A6

Planck Collaboration, 2014b, *A&A*, 571, A11

Richter, P., 2017, in A. Fox & R. Davé, eds., *Gas Accretion onto Galaxies, Astrophysics and Space Science Library*, volume 430, 15

Schlafly, E. F., et al., 2014, *ApJ*, 786, 29

Schlegel, D. J., Finkbeiner, D. P., & Davis, M., 1998, *ApJ*, 500, 525

Smith, G. P., 1963, *Bull. Astron. Inst. Netherlands*, 17, 203

Snowden, S. L., Freyberg, M. J., Kuntz, K. D., & Sanders, W. T., 2000, *ApJS*, 128, 171

Snowden, S. L., Mebold, U., Hirth, W., Herbstmeier, U., & Schmitt, J. H. M., 1991, *Science*, 252, 1529

Snowden, S. L., et al., 1997, *ApJ*, 485, 125

Sofue, Y., Kudoh, T., Kawamura, A., Shibata, K., & Fujimoto, M., 2004, *PASJ*, 56, 633

Takahira, K., Tasker, E. J., & Habe, A., 2014, *ApJ*, 792, 63

van Woerden, H., Wakker, B. P., Schwarz, U. J., & de Boer, K. S., eds., 2004, *High Velocity Clouds, Astrophysics and Space Science Library*, volume 312

Wakker, B. P., 2001, *ApJS*, 136, 463

Wakker, B. P., & van Woerden, H., 1997, *ARA&A*, 35, 217

Walborn, N. R., 1976, *ApJ*, 205, 419

Yamamoto, H., Onishi, T., Mizuno, A., & Fukui, Y., 2003, *ApJ*, 592, 217

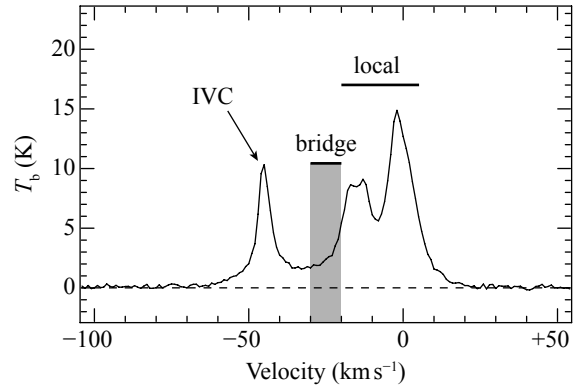


Fig. 1. A typical profile of the HI in the MBM53–55/IVC 86–36 region. The component of the IVC, bridge and local gas are represented in the figure.

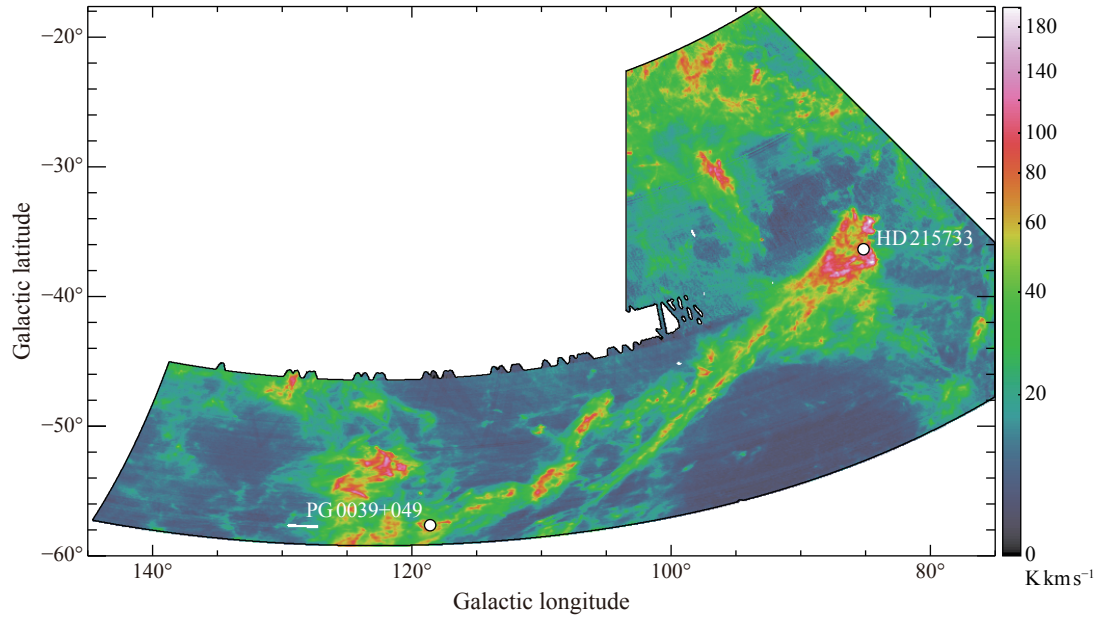


Fig. 2. The HI distribution of the IVC 86–36 integrated over a velocity range from -80 km s^{-1} to -30 km s^{-1} . The position of PG0039+049 and HD215733 is shown in the figure.

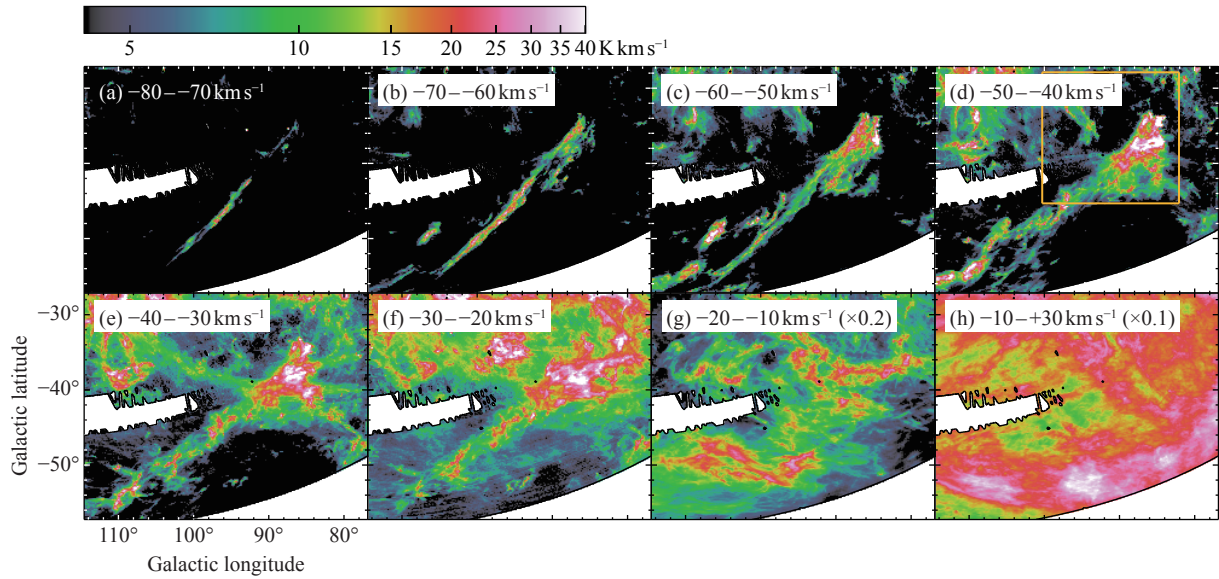


Fig. 3. The velocity channel maps of the HI every 10 km s^{-1} from -80 km s^{-1} to $+30 \text{ km s}^{-1}$. The velocity-integrated intensity in (g) and (h) is multiplied by 0.2 and 0.1, respectively. The bounding box in (d) indicates the region shown in Figure 6.

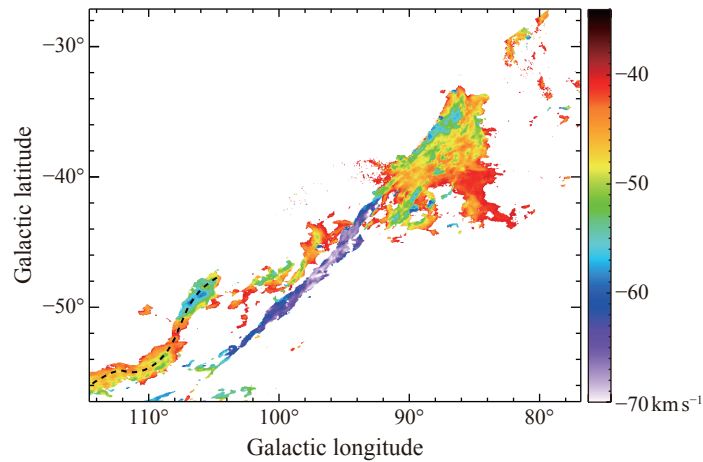


Fig. 4. The first moment map of the HI calculated in a velocity range from -70 km s^{-1} to -35 km s^{-1} . The winding structure described in the text is shown by a dashed line.

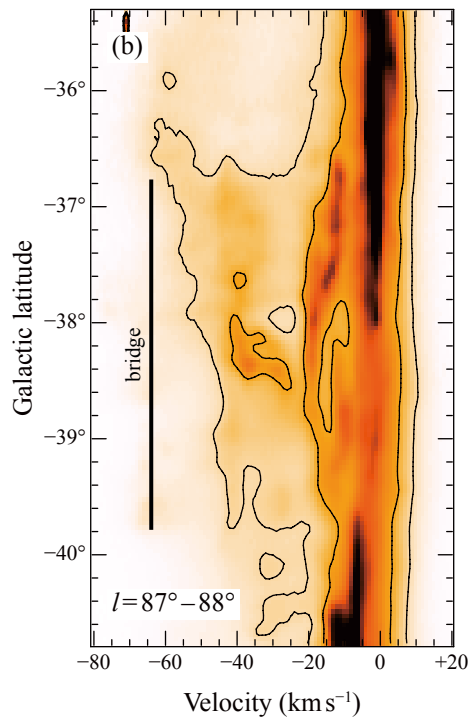
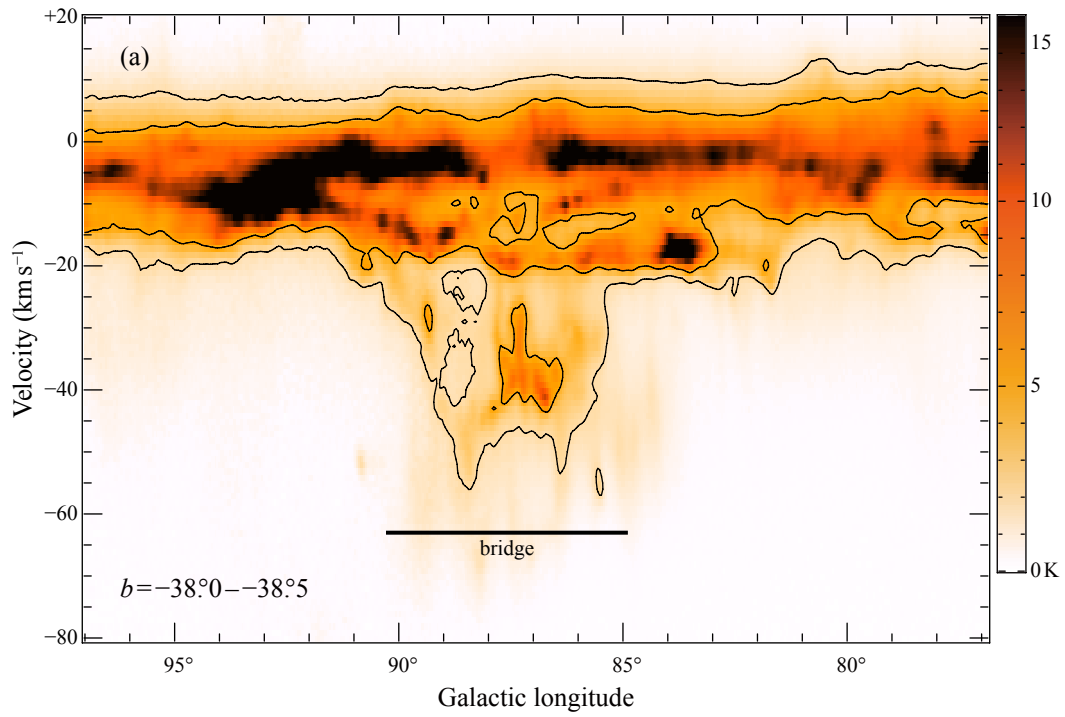


Fig. 5. The Galactic longitude-velocity diagram (a) and the velocity-Galactic latitude diagram (b) in the H_I. The intensity is averaged over each Galactic latitude and longitude in (a) and (b), respectively. The contour levels in both (a) and (b) are 2 K and 5 K. The position of bridge feature is shown in the figures.

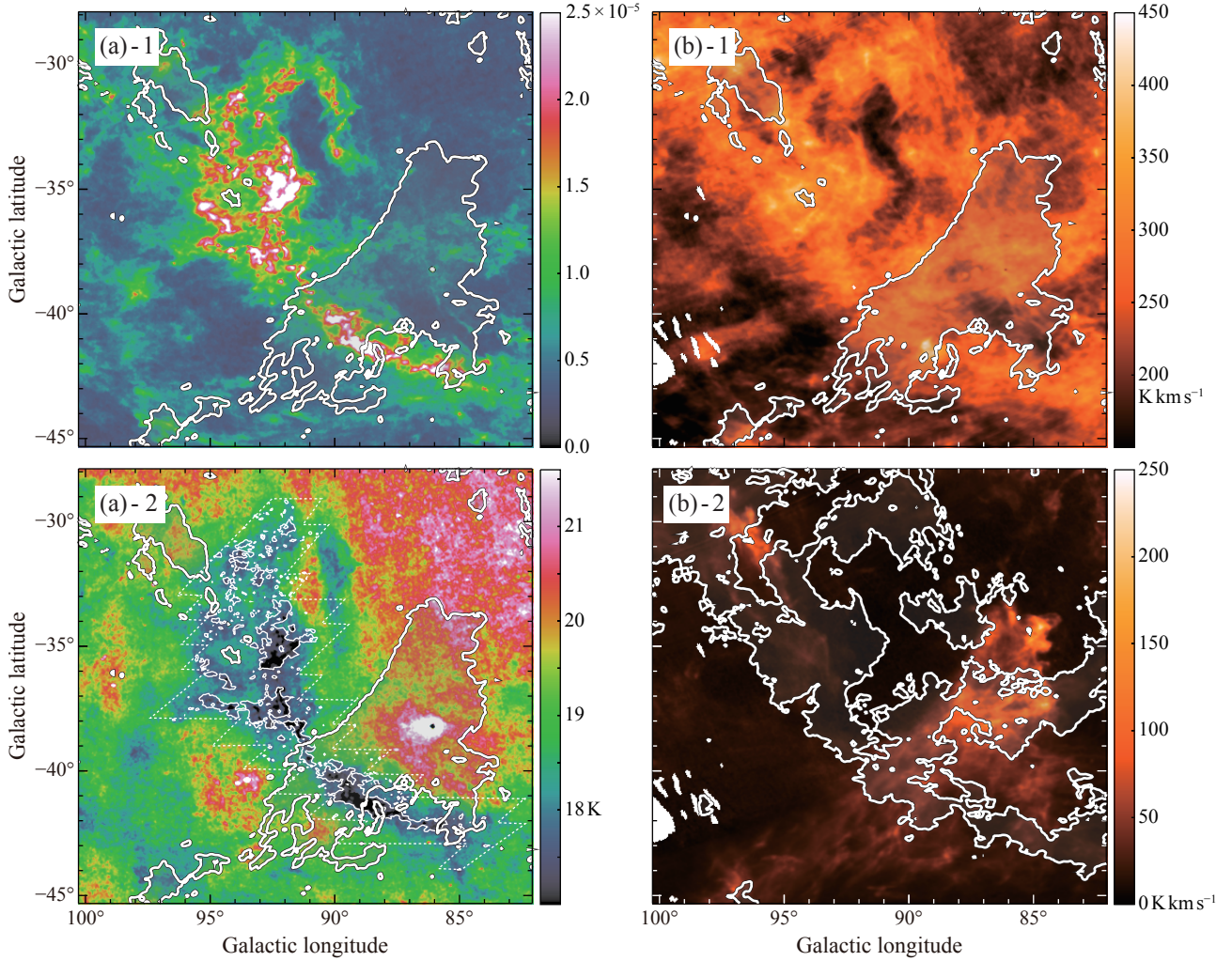


Fig. 6. (a) Spatial distributions of τ_{353} ((a)-1) and T_d ((a)-2) (Planck Collaboration 2014b). (b) Those of W_{HI} integrated in a velocity range from -30 km s^{-1} to $+30 \text{ km s}^{-1}$ ((b)-1) and from -60 km s^{-1} to -30 km s^{-1} ((b)-2). The gray-shades outlined by thick contours in panels (a)-1, (a)-2 and (b)-1 show the distribution of the IVC and that in panel (b)-2 show the local ISM. The thin contours in panel (a)-2 show spatial distribution of ^{12}CO (using the same dataset as Figure 1(a) of Fukui et al. 2014) integrated in a velocity range from -12 km s^{-1} to $+2 \text{ km s}^{-1}$.

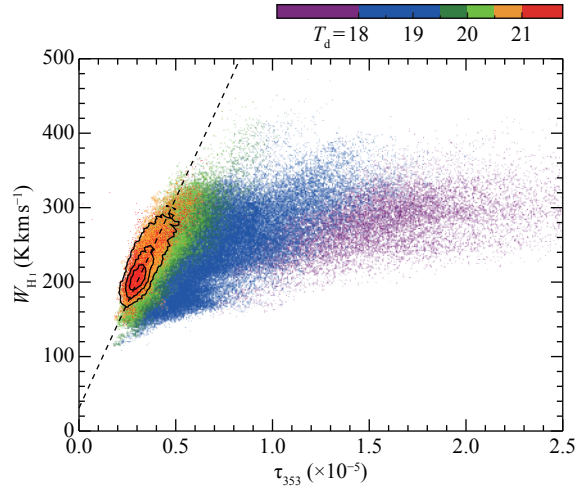


Fig. 7. Scatter plot between τ_{353} and W_{HI} for the local ISM (W_{HI} are integrated from -30 to $+30\text{ km s}^{-1}$). Color represents T_d of each point. The contours include 30%, 60%, and 90% of data points with $T_d > 20.5\text{ K}$ and the dashed line is linear regressions for the data points.

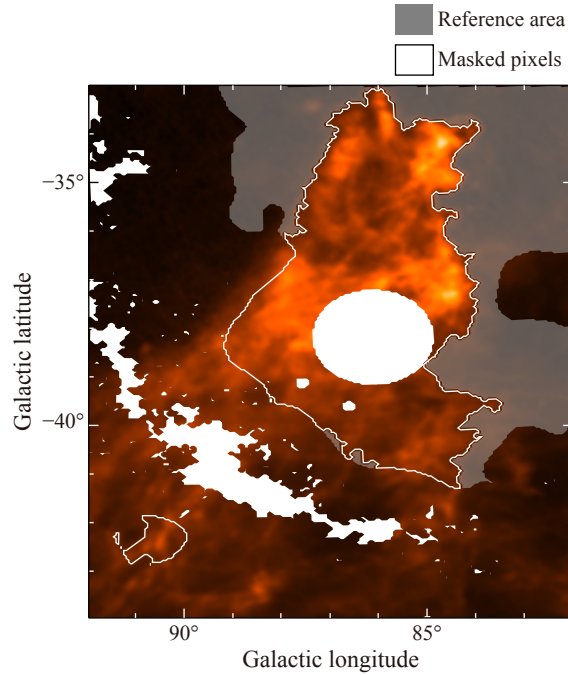


Fig. 8. The area of IVC 86–36 head (outlined by the white line) and the reference area (the gray shaded are) used in the following analyses. White shows the masked pixels where CO emission is higher than 1.1 K km s^{-1} or high T_d indicating localized heating by point sources (see section 2.5 of Fukui et al. 2014).

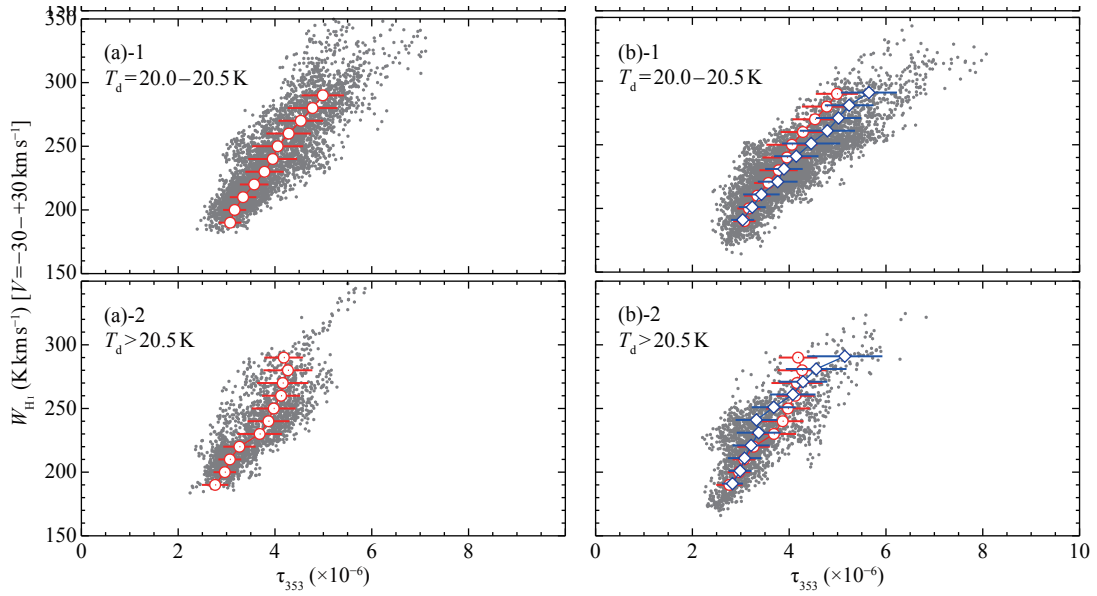


Fig. 9. (a) Scatter plots between W_{HI} integrated in a velocity range from -30 to $+30 \text{ km s}^{-1}$ versus τ_{353} in the reference area. Each panel shows for T_{d} ranges of $20.0 - 20.5 \text{ K}$ ((a)-1), and $T_{\text{d}} > 20.5 \text{ K}$ ((a)-2). The red circles and horizontal bars are the average and standard deviation of τ_{353} in each 10 K km s^{-1} bin. (b) Same as (a) but for the area of IVC 86–36 head. The blue diamonds and bars are the average and standard deviation of τ_{353} . The red circles and bars identical to those in the Panels (a)-1,2 are superimposed for comparison.

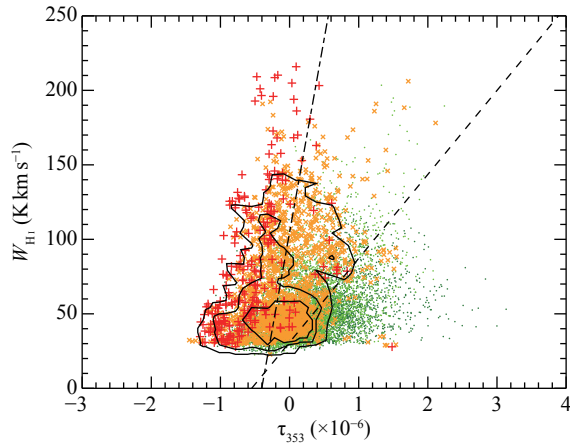


Fig. 10. Scatter plot between τ_{353} and W_{HI} for the area of IVC 86–36 head. τ_{353} are corrected following a procedure described in Section 4.2 and W_{HI} are integrated in a velocity range from -60 to -30 km s^{-1} . The orange x-marks are data points with $T_{\text{d}} = 20.5 - 21.0 \text{ K}$ and the red crosses are $T_{\text{d}} > 20.5 \text{ K}$. The contours include 30%, 60%, and 90% of data points and the dash-dotted line is linear regressions. The regression line for the local ISM (Figure 7) is shown by the dashed line.

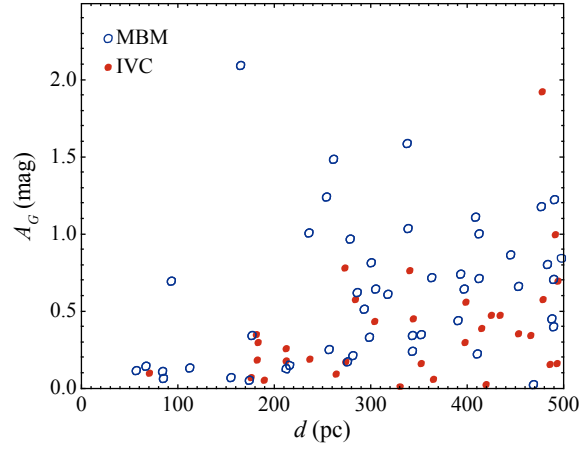


Fig. 11. The extinction A_G against the distance for the GAIA sources sampled from the fields in the IVC (filled circles) and in MBM 53 (open circles). The positions of the fields are listed in Appendix 1.

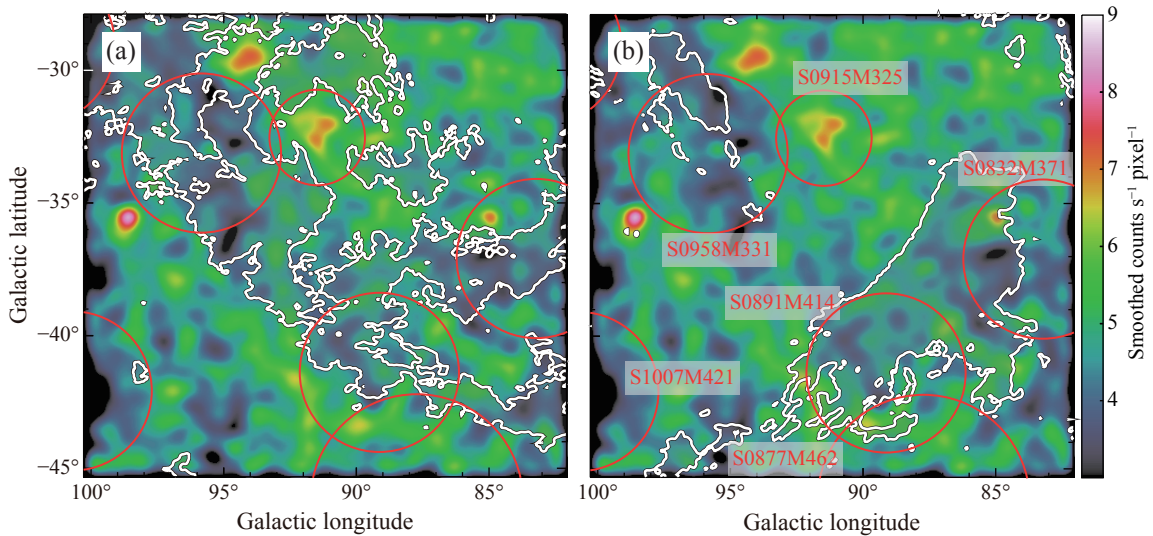


Fig. 12. ROSAT R1 band image toward MBM53–55/IVC 86–36 region. The image is regridded to same projection type and pixel size ($2'.4$) as dust and HI maps in Figure 6, and smoothed with a Gaussian function. The circles show position and size of X-ray shadows in the catalog of Snowden et al. (2000). The gray-shades outlined by contours in panel (a) show the distribution of the local ISM and those in panel (b) show the IVC.